

## Research Article

# Aerodynamic Analysis of a Manned Space Vehicle for Missions to Mars

Giuseppe Pezzella<sup>1</sup> and Antonio Viviani<sup>2</sup>

<sup>1</sup>Fluid Dynamics Laboratory, Aerothermodynamics Division, Centro Italiano Ricerche Aerospaziali (CIRA),  
Via Maiorise, 81043 Capua, Italy

<sup>2</sup>Dipartimento di Ingegneria Aerospaziale e Meccanica (DIAM), Seconda Università di Napoli (SUN),  
Via Roma 29, 81031 Aversa, Italy

Correspondence should be addressed to Giuseppe Pezzella, g.pezzella@cira.it

Received 3 November 2010; Accepted 7 January 2011

Academic Editor: L. De Goeij

Copyright © 2011 G. Pezzella and A. Viviani. This is an open access article distributed under the Creative Commons Attribution License, which permits unrestricted use, distribution, and reproduction in any medium, provided the original work is properly cited.

The paper deals with the aerodynamic analysis of a manned braking system entering the Mars atmosphere with the aim to support planetary entry system design studies. The exploration vehicle is an axisymmetric blunt body close to the Apollo capsule. Several fully three-dimensional computational fluid dynamics analyses have been performed to address the capsule aerodynamic performance. To this end, a wide range of flow conditions including reacting and nonreacting flow, different angles of attack, and Mach numbers have been investigated and compared. Moreover, nonequilibrium effects on the flow field around the entry vehicle have also been investigated. Results show that real-gas effects, for all the angles of attack considered, increase both the aerodynamic drag and pitching moment whereas the lift is only slightly affected. Finally, results comparisons highlight that experimental and CFD aerodynamic findings available for the Apollo capsule in air adequately represent the static coefficients of the capsule in the Mars atmosphere.

## 1. Introduction

The paper deals with the aerodynamic analysis of a manned braking system (MBS) entering the Mars atmosphere with the aim to support planetary entry system design studies.

The human exploration of Mars will be a complex undertaking. It is an enterprise that will confirm the potential for humans to leave our home planet and make our way outward into the cosmos. Though just a small step on a cosmic scale, it will be a significant one for humans, because it will require leaving Earth with very limited return capability. The commitment to launch is a commitment to several years away from Earth, and there is a very narrow window within which return is possible. This is the most radical difference between Mars exploration and previous lunar explorations [1].

The paper reports on some aerodynamic analysis of an Apollo-shaped vehicle performed for flight conditions compatible for a manned mission entering the Mars atmosphere. With this in mind, those results may be used to provide

numerical data for understanding requirements for human exploration of Mars. To this end, aerodynamic analysis has been made at several levels. For instance, vehicle aerodynamic assessment has been extensively addressed through an engineering-based design approach as hypersonic panel methods. Then, a number of computational fluid dynamics (CFD) simulations of the hypersonic flow field past the entry capsule have been performed, and results were provided in the paper.

The reasons that suggest getting the Mars manned exploration ready are several. Mars is the most accessible planet beyond the Earth-Moon system where sustained human presence is believed to be possible. The technical objectives of Mars exploration should be to understand what would be required to sustain a permanent human presence beyond Earth. Moreover, the scientific objectives of Mars exploration should be to investigate the planet and its history to better understand Earth. The human exploration of Mars currently lies at the ragged edge of achievability. The necessary technical capabilities are either just available

or on the horizon. Commitment to the program will both effectively exploit previous investments and contribute to advances in technology. Finally, the goals of Mars exploration are grand; they will motivate our youth, benefit technical education goals, and excite the people and nations of the world.

The crew will travel to and from Mars on relatively fast transits (4 to 6 months) and will spend long periods of time (18 to 20 months: days nominal) on the surface, rather than alternative approaches which require longer time in space and reduced time on the surface [1]. Figure 1 illustrates a typical trajectory designed for the worst-case mission opportunity (2007–2009) of the next two decades, the transit legs are less than 180 days, both directions. For easier Mars mission opportunities (e.g., 2016–2018), the transit legs are on the order of 130 days. Shorter transit times reduce the time spent by crew in zero g to the length typical of the duty for the International Space Station [1].

In the paper, however, neither mission architecture needed to reach Mars from Earth or neighbour Earth space, nor surface exploration have been addressed. Only capsule aerodynamics in Mars atmosphere have been focused on. In this framework, fully three-dimensional CFD analyses, both Euler and Navier-Stokes, have been performed to address the aerodynamic performance of the exploration vehicle, considering an entry approach scenario to the red planet compliant with the spacecraft released from circular parking orbit [2, 3]. Today, the need for research activities on Mars entry are ever more apparent, and among the available technologies, capsule option is still the safest and cheapest way to get exploration vehicle on Mars [4, 5].

The Martian atmosphere has been considered as a mixture of 95.7% carbon-dioxide, 1.6% argon, and 2.7% nitrogen. The flow has been modelled as a reacting gas mixture of 9 species (Ar, CO<sub>2</sub>, N<sub>2</sub>, O<sub>2</sub>, CO, NO, N, O). The fluent code together with user-defined functions, developed in order to simulate mixtures of gas in thermochemical nonequilibrium, has been used for CFD computations with a nonequilibrium chemical model suitable for Martian atmosphere [6]. Several numerical computations have been performed in order to obtain pressure distributions and other several flow field features both over and around the entry vehicle for the aerodynamic system design analysis scopes. Therefore, a wide range of flow conditions including reacting and nonreacting flow, different angles of attack, and Mach numbers have been investigated and compared. Moreover, 3D numerical simulations have been carried out to investigate the effects of chemical nonequilibrium on the vehicle aerodynamics. For code validation purposes, the available numerical and experimental data of the Mars Pathfinder probe at the entry peak heating conditions have been used [7]. The comparison has shown good agreement between numerical and experimental data.

## 2. The Mars Manned Entry Braking Vehicle

The MBS configuration, under investigation in this work, is shown in Figure 2. It consists of a blunt body close to an Apollo-shaped capsule measuring about 5 m in diameter,

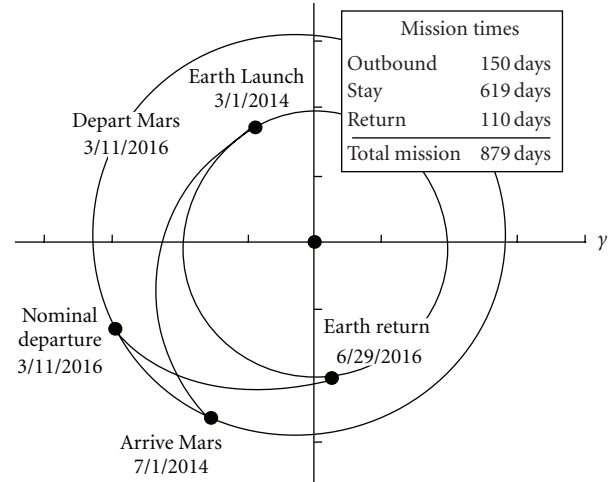


FIGURE 1: Typical fast-transit interplanetary trajectory to Mars and return [1].

with a nose radius of 6.05 m, a sidewall angle of 33 deg, and an overall height of 3.8 m.

Such a system design choice has been addressed in order to reduce overall development cost and design risk. In fact, capsule technology is still the safest and cheapest way to get an exploration crew into orbit and then entry to planetary atmosphere as in the case of Mars. Moreover, even if the configuration is essentially ballistic, the vehicle is able to exhibit lifting capabilities by offsetting the centre of gravity (CoG). Note that the aerodynamic lift capability is fundamental for range extension and manoeuvrability in the descent and landing phases, since lift permits the correction of errors occurring in the guidance, navigation, and control systems, thus attaining the desired landing site in spite of such errors. In addition, aerodynamic lift gives desirable advantages in the form of operational flexibility in the positioning of the line of nodes of the parking orbit and in maximizing the time available for performing the deorbit manoeuvre.

## 3. The Mars Manned Entry Scenario and Freestream Conditions of Aerodynamic Analysis

Generally speaking, the MBS design depends on mission flight scenario requirements, which define capsule entry corridor. For instance, the entry corridor envelopes all the flyable/admissible entry trajectories whose loading environment is tolerable by the capsule. It is bounded from one side by the peak heat flux and the maximum deceleration, from the other by the ablator thermal limitations (total heat load), if present, and the skip angle. The dispersion of the trajectory within the entry corridor depends on two main design parameters that are the entry flight path angle and velocity, which are characterized by the selected planetary approach trajectory. Indeed, the angle and the velocity at entry interface determine the time of permanence

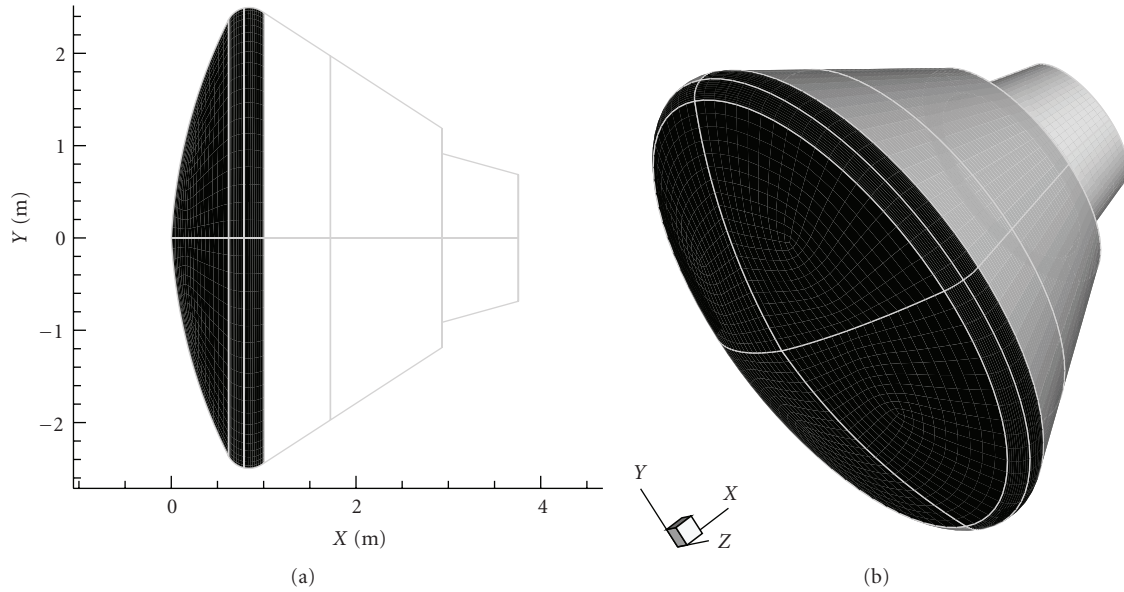


FIGURE 2: The manned braking system.

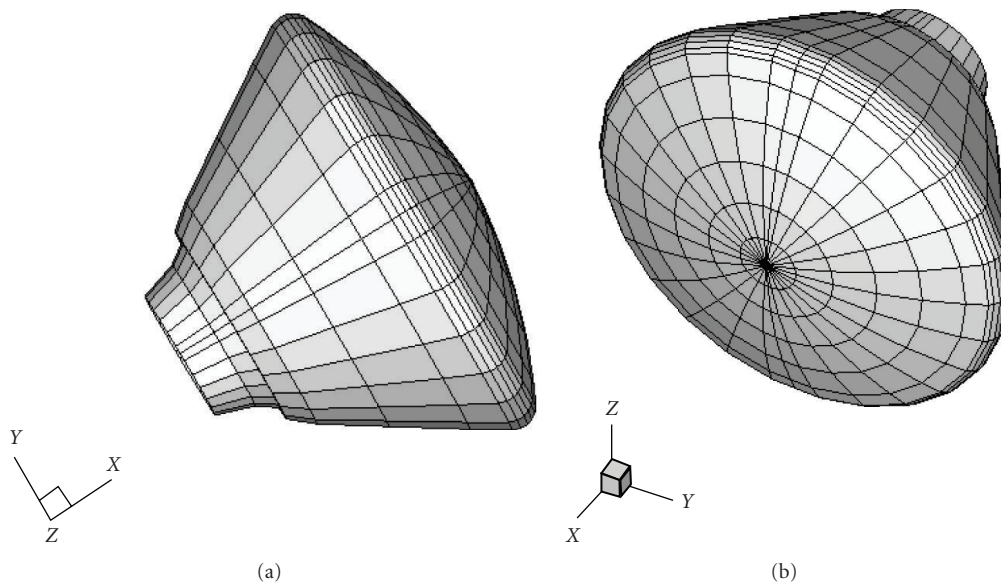


FIGURE 3: The MBS panel mesh.

in the Martian atmosphere. The shallower the entry angle, the bigger the flight time and the dispersion due to the atmospheric model error, and, hence, the worse the landing accuracy. From the point of view of approach strategies, the different values of velocity at entry interface (given the entry angle) will characterize the MBS design by means of mechanical loads (i.e., pressure and acceleration), thermal loads (i.e., heat flux peak and integrated heat load), and landing dispersion. These parameters counterbalance with each other, in the sense that the higher the entry velocity (or the steeper the entry angle), the larger the deceleration during the descent path (higher structure solicitations), and the higher the heat flux peak (higher TPS solicitations).

Moreover, the lower the entry velocity (or the shallower the entry angle), the bigger the total heat flux (thicker ablative materials layer), the longer the atmospheric flight time, hence, the higher the landing dispersion (bigger atmospheric model errors).

In this paper, the flight scenario refers to entry conditions compatible with a capsule released from Mars parking orbit that the overall expedition system to Mars achieves after the red planet capture through aerobraking maneuvers.

With this in mind, fully three-dimensional CFD simulations both for perfect and chemically reacting gas approximation have been computed, according to the space-based design approach, at the freestream conditions listed in

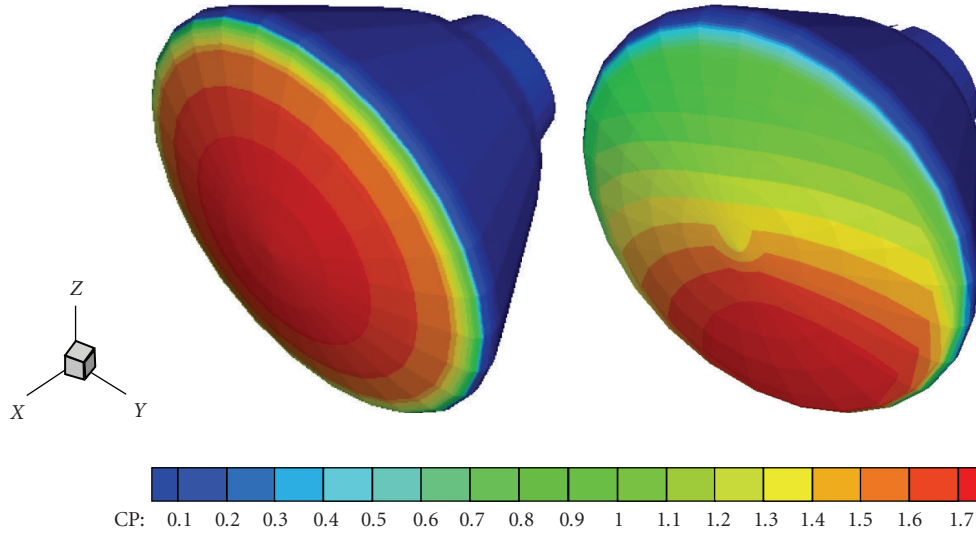


FIGURE 4: Pressure coefficient contours on MBS surface at  $\alpha = 0$  deg (left) and at  $\alpha = 25$  deg (right) for  $M_\infty = 20$ .

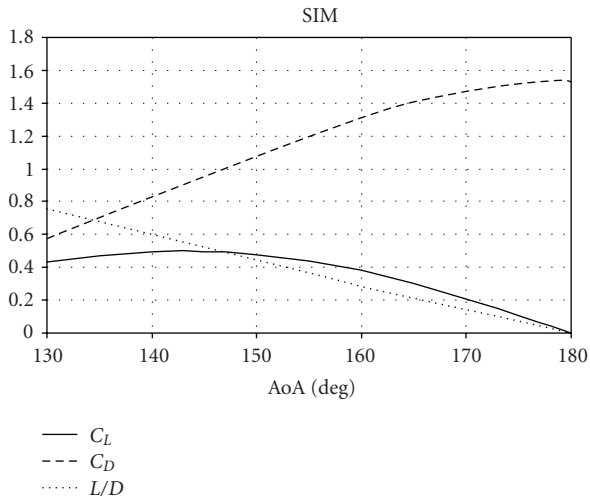


FIGURE 5: Lift, drag, and  $L/D$  ratio coefficients versus  $\alpha$ . Panel methods results.

TABLE 1: Freestream conditions of CFD computations.

Mach (-)	Pressure (Pa)	Temperature (k)	AoA (deg)
5	1400	560	10
10	1400	560	10
20	1400	560	20
20	1400	560	28

Table 1 and for laminar flow conditions only [8]. Several Mach numbers and different angles of attack  $\alpha$  have been investigated and compared. Note that, for the perfect gas case, the Mars atmosphere is characterized by a specific heats ratio  $\gamma$  (e.g., 1.3755) very close to that of Earth (e.g.,  $\gamma = 1.4$ ). Therefore, it follows that force coefficients are nearly independent of  $\text{CO}_2$  concentration and are essentially the same as those obtained using air.

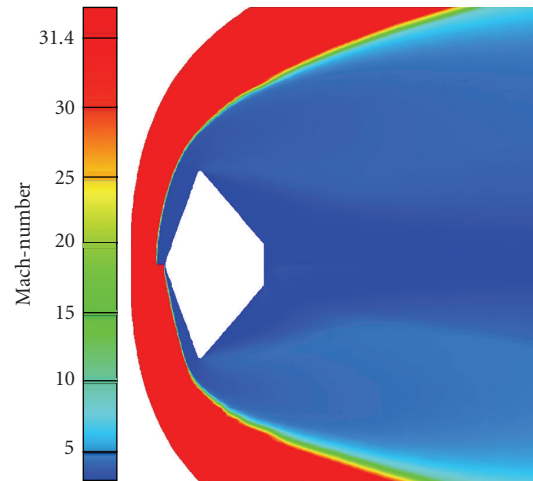


FIGURE 6: Mars Pathfinder. Mach number contours at trajectory peak heating conditions. Comparison between perfect gas (upper side) and equilibrium flow. Axisymmetric computation.

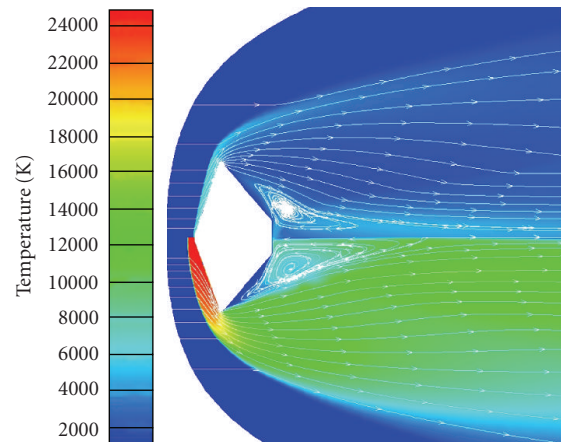


FIGURE 7: Mars Pathfinder. Temperature contours at trajectory peak heating conditions. Comparison between perfect gas (upper side) and equilibrium flow. Axisymmetric computation.

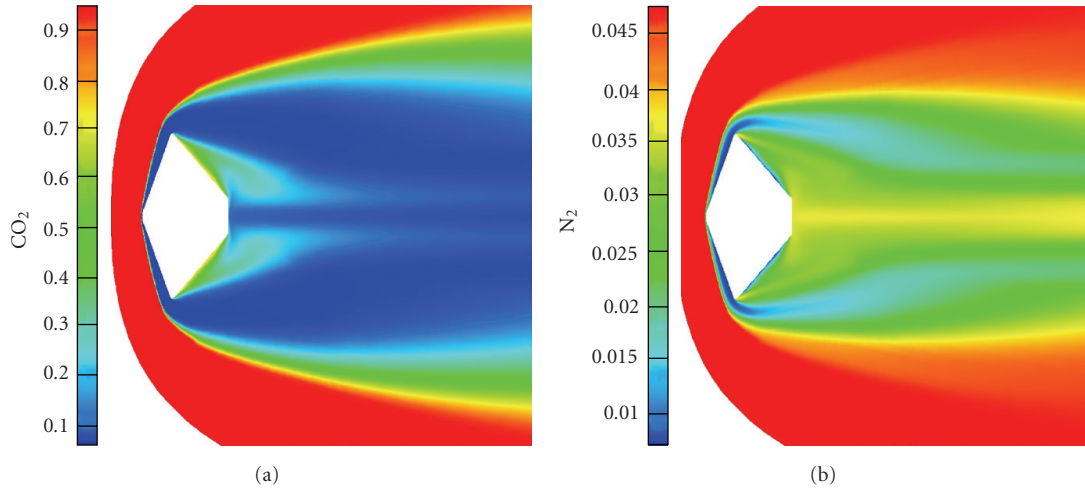


FIGURE 8: Mars Pathfinder. Contours of CO<sub>2</sub> and N<sub>2</sub> mass fractions at trajectory peak heating conditions. Axisymmetric computation.

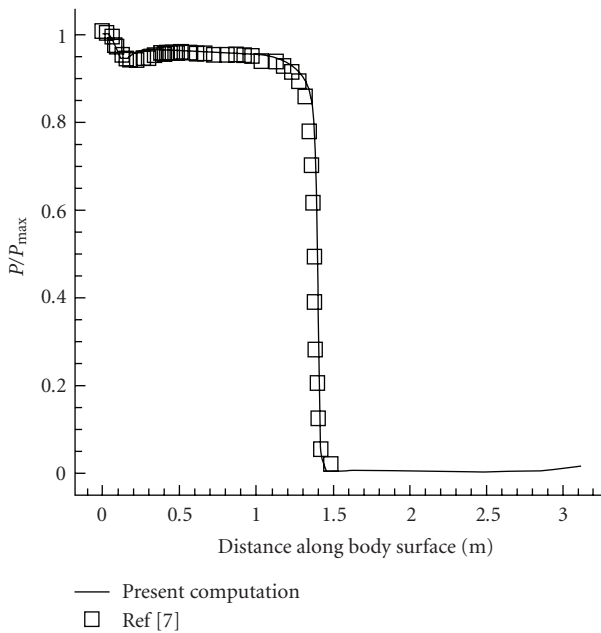


FIGURE 9: Mars Pathfinder. Comparison of surface pressure to stagnation pressure ratio between present computation and results of [7].

Moreover, also nonequilibrium computations have been performed, since, as it is well known, one of the most challenging problems facing the design of atmospheric entry vehicle is the phenomenon of “real gas behaviour”. For instance, the shock wave produced ahead of the vehicle travelling at hypersonic speeds suddenly elevates the temperature of the gas surrounding the vehicle, so that the thermal energy of the gas may be comparable with the energy associated with a whole range of gas phase chemical processes, such as the excitation of molecular modes of vibration; the dissociation of atmospheric molecules into their atomic forms; the formation of other chemical species

through recombination reactions; the ionisation of both molecular and atomic species [9].

Since the ratio between the specific heats ( $\gamma$ ) depends on the number of active degrees of freedom of the species, it is evident that as the temperature increases, the value of  $\gamma$  cannot be considered as a constant (perfect gas hypothesis). Therefore, the gas mixture has to be considered in thermal and chemical nonequilibrium.

Further, the “real gas effects” play a relevant role in the thermodynamics of the flow around the vehicle. For example, thermodynamic equilibrium is not established instantaneously in the moving gas, but requires a finite time known as relaxation time. Departure from thermodynamic equilibrium can have significant effects on shock wave structure, thus affecting the flow field around the vehicle [10].

The chemical dissociation of the flow in the shock layer can result in a large density ratio  $\varepsilon$  across the strong bow shock compared with a flow of the same gas where no dissociation takes place [9]. Under conditions where dissociation exists, the aerodynamics of capsules depend primarily on shock density ratio. In fact, the change of aerodynamic characteristics is the result of change in surface pressure acting on the vehicle forebody [11].

Further, both the shock shape and standoff distance are markedly influenced by  $\varepsilon$ . The surface pressures are affected by a change in shock density ratio, because the level of pressure at the stagnation point (e.g.,  $C_{p_{\max}}$ ) is changed:

$$C_{p_{\max}} = C_{pt2} = \frac{P_{t2} - P_{\infty}}{q_{\infty}} = \left( \frac{P_{t2}}{P_{\infty}} - 1 \right) \frac{2}{\gamma M_{\infty}^2} \cong 2 - \varepsilon \quad (1)$$

instead of the classical Newtonian value of  $C_{p_{\max}} = 2$ , where the density ratio across the bow shock wave,  $\varepsilon$ , in the hypersonic limit reads

$$\varepsilon = \lim_{M_{\infty} \rightarrow \infty} \frac{\rho_1}{\rho_2} = \frac{\gamma - 1}{\gamma + 1}. \quad (2)$$

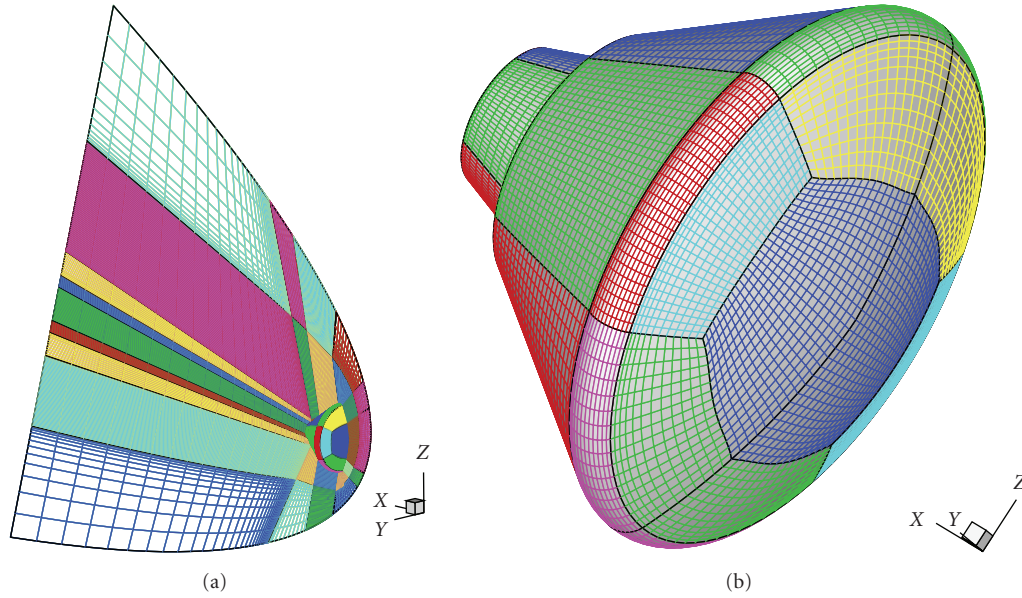
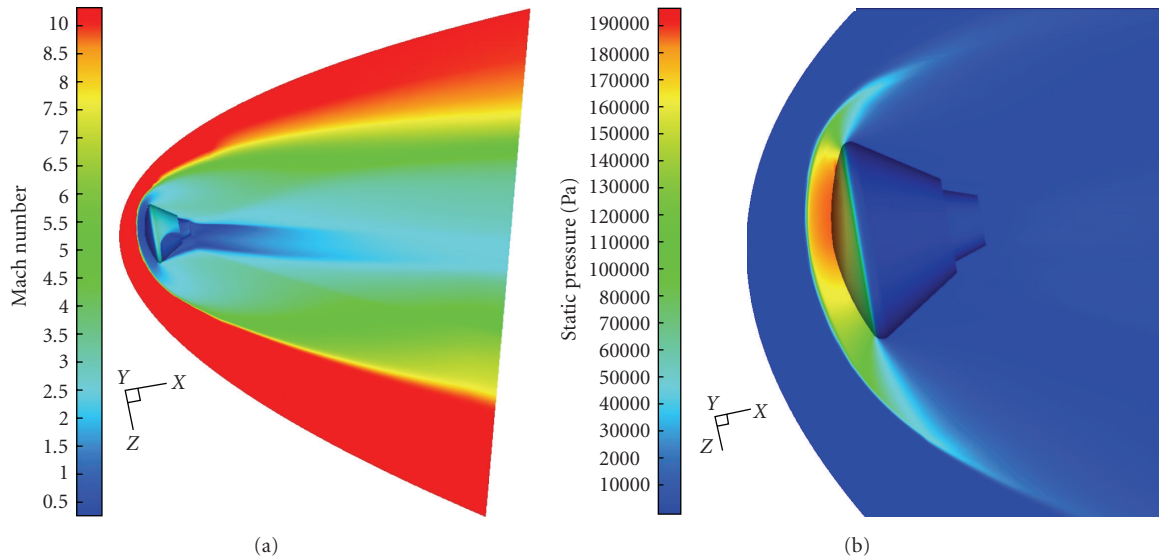


FIGURE 10: The computational domain.

FIGURE 11: Mach number (a) and static pressure contours for  $M_\infty = 10$  and  $\alpha = 10$  deg.

Moreover, the nondimensional distribution of surface pressure relative to stagnation point pressure is changed as highlighted by numerical results collected hereinafter.

The sonic line position shifts because of the change in  $\gamma$  [11]. Therefore, as static aerodynamic instability depends on the sonic line location, high-temperature effects result in modifying vehicle hypersonic aerodynamics and aerothermodynamics by means of a very abrupt change in the trim angle of the capsule [12].

Body stability is a critical requirement for re-entry vehicle, because of static instability could lead to catastrophic failure if the thermal shield is not protecting the vehicle

anymore. This is the explanation of the relation that exists between pitching moment coefficient ( $C_{MY}$ ) and sonic line location. For instance, the change of  $C_{MY}$  is associated to the motion of the sonic line location on vehicle lee side.

In order to address the real gas effects, the Martian atmosphere has been considered as a reacting gas mixture of nine species (Ar, CO<sub>2</sub>, N<sub>2</sub>, O<sub>2</sub>, CO, NO, N, O) involved in 49 forward and backward chemical reactions [13–15]. The reaction mechanism and the related chemical kinetics, taken into account in the present nonequilibrium CFD computations, are summarized in Table 2, where  $M$  is the reacting partner (third body) that can be any of the nine

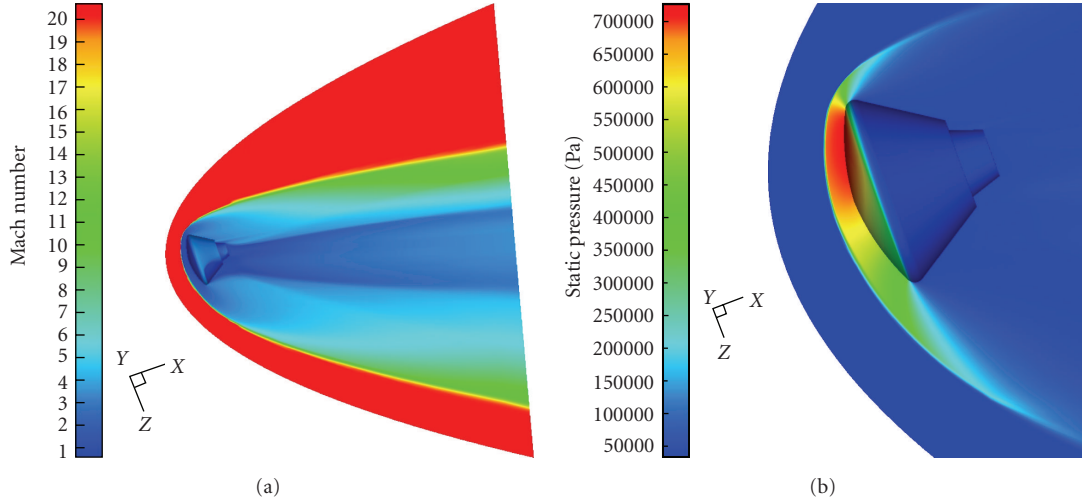


FIGURE 12: Mach number (a) and static pressure contours for  $M_\infty = 20$  and  $\alpha = 20$  deg.

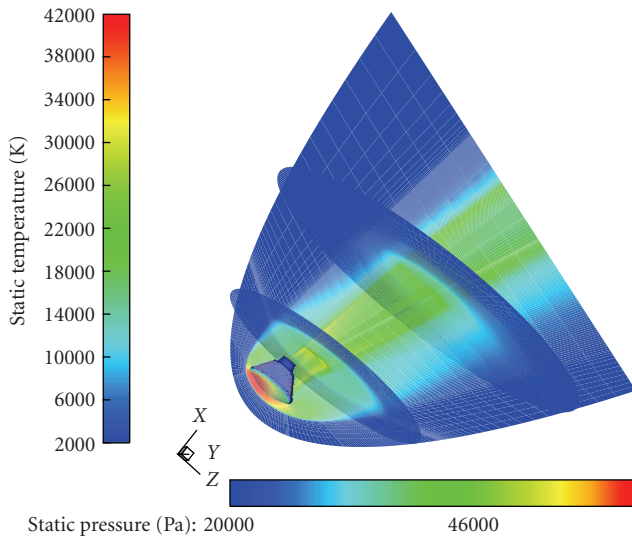


FIGURE 13: The static temperature field on the capsule symmetry plane and on two flow field cross-sections at  $M_\infty = 20$  and  $\alpha = 20$  deg. Static pressure contour on capsule forebody.

reacting species. Both reaction mechanism and kinetics are derived by those suggested by Park et al. in [13].

Note that this reaction scheme neglects ionic reactions since the degree of ionization is expected to be low in the environment of interest (e.g., entry below 9 km/s), as suggested by Park et al. in [13] due to the presence of  $\text{CO}_2$ ,  $\text{N}_2$ , and Ar in the Martian atmosphere.

#### 4. Numerical Results

The aerodynamic analysis of MBS is shown in terms of lift ( $C_L$ ), drag ( $C_D$ ), and pitching moment ( $C_{M_y}$ ) coefficients

which are calculated according to the following:

$$C_i = \frac{F_i}{(1/2)\rho_\infty v_\infty^2 S_{\text{ref}}}, \quad i = L, D, \quad (3)$$

$$C_{M_j} = \frac{M_j}{(1/2)\rho_\infty v_\infty^2 L_{\text{ref}} S_{\text{ref}}}, \quad j = Y.$$

The reference parameters that have been chosen for the definition of the aerodynamic forces and moment nondimensional coefficients are the longitudinal reference length ( $L_{\text{ref}} = D = 2R_b$ ), equal to the capsule diameter (e.g., 5.0 m), and the reference surface ( $S_{\text{ref}} = \pi R_b^2 = 19.6 \text{ m}^2$ ), that is the maximum cross-section area of the MBS. The pitching moment is computed from the nose of the capsule vehicle.

The evaluations of the vehicle aerodynamic database (AEDB) has been performed by means of engineering tools and CFD computations to focus on some critical design aspects not predictable with simplified tools as, for example, real gas effects.

**4.1. Engineering-Based Results.** Engineering-based aerodynamic and aerothermodynamic analyses have been extensively performed by using a 3D Panel Methods code, namely, SIM (surface impact method) developed by CIRA in the frame of its research activities on preliminary design of re-entry vehicles. This tool, at high supersonic and hypersonic speeds, is able to accomplish the aerodynamic and aerothermodynamic analyses of a complex vehicle configuration by using simplified approaches as local surface inclination methods and approximate boundary-layer methods, respectively. The SIM typical of hypersonics are Newtonian and Modified Newtonian theories. In Figure 3, a typical mesh surface of the MBS, used for the engineering level computations, is shown.

MBS aerodynamic results provided by engineering-based analysis cover  $\alpha$  ranging from 130 to 180 deg. It is worth noting that the AoA is measured from the capsule apex, as done in the past for Apollo command module.

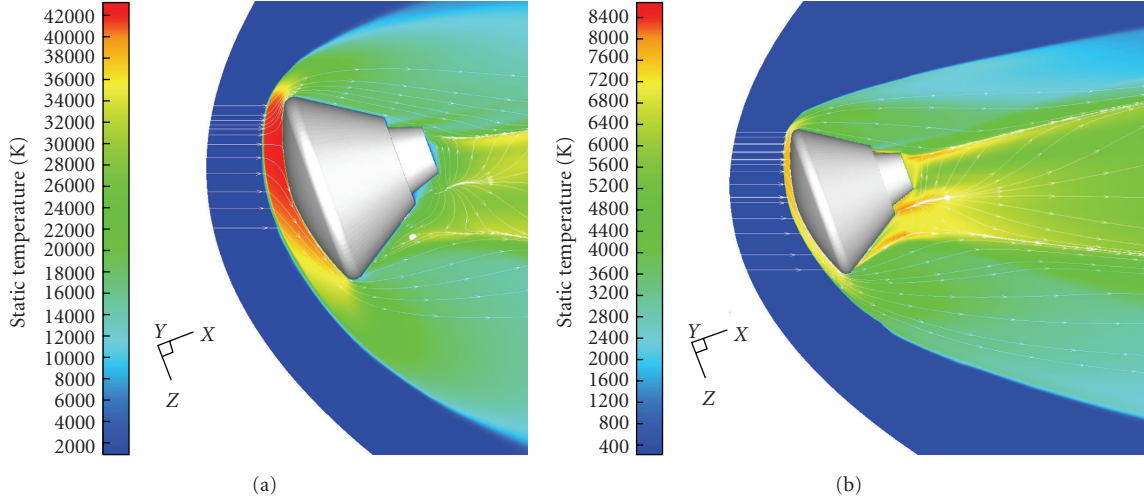


FIGURE 14: Static temperature contours for  $M_\infty = 20$  and  $\alpha = 20$  deg. Comparison between perfect gas (a) and nonequilibrium gas (b) computations.

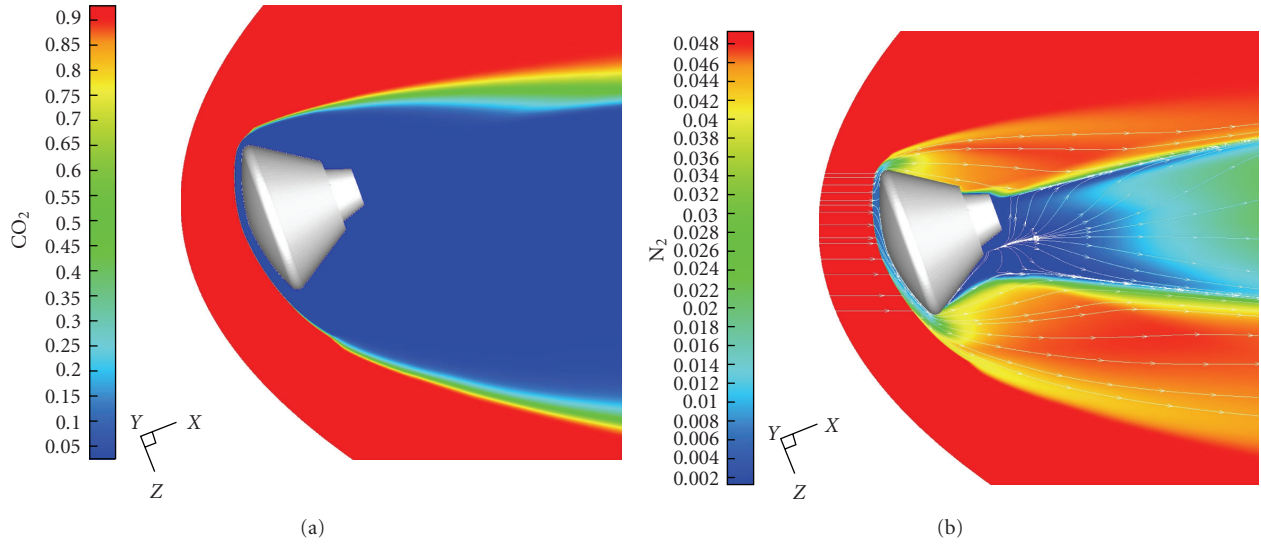


FIGURE 15: Contours of  $\text{CO}_2$  and  $\text{N}_2$  mass fractions on the MBS pitch plane.

As an example of SIM results, Figure 4 shows the contours of pressure coefficient over the capsule surface at  $\alpha = 0$  deg (left) and at  $\alpha = 25$  deg (right) for  $M_\infty = 20$ .

The curves of lift, drag, and aerodynamic efficiency are shown in Figure 5. It collects MBS aerodynamic coefficients which represent the preliminary aerodynamics assessment of Mars entry capsule.

**4.2. Computational Fluid Dynamics Results.** Computational fluid dynamics analyses are performed to simulate the flow field past the entering vehicle to assess MBS aerodynamic performance. Both perfect gas and reacting gas with finite rate chemistry models (see Table 2) are used in fully three-dimensional Euler and Navier-Stokes computations. All the results reported in the paper refer to laminar steady-state CFD simulations started at the freestream conditions

summarized in Table 1 as initial conditions. Further, all the simulations have been performed assuming the vehicle surface as a fully catalytic wall and its temperature ( $T_w$ ) at radiative equilibrium condition. Therefore, during numerical simulations, the wall temperature is calculated by the Stephan-Boltzman law, and it is explicitly updated at each streamwise station by means of the Newton-Raphson approach. As a consequence, the energy balance at vehicle surface (neglecting the heat conduction inside the wall) reads

$$\dot{q}_w = -\lambda \left( \frac{\partial T}{\partial n} \right)_w - \rho \sum_i D_{im} h_{Di} \left( \frac{\partial Y_i}{\partial n} \right)_w = \sigma \varepsilon T_w^4 \quad (4)$$

The first term is the conductive heat-flux from fluid to the wall due to the temperature gradient. The second one is the diffusion term due to the species gradient. The

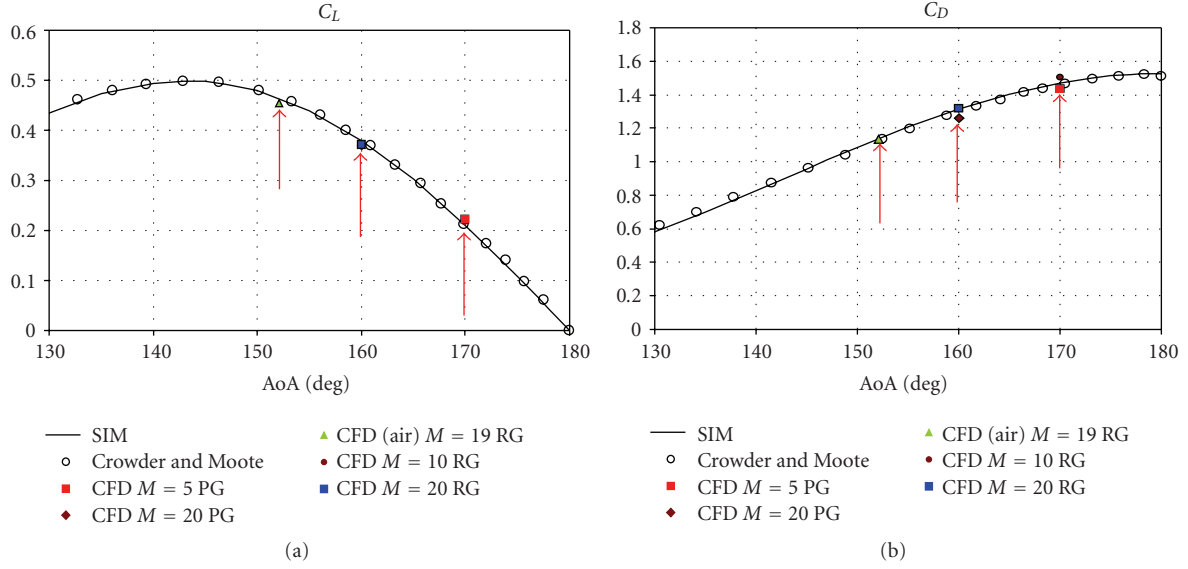


FIGURE 16: Lift and drag coefficients versus  $\alpha$ . Comparison among panel methods, CFD results, and experimental data [16].

TABLE 2: Reactions mechanism and rate parameters.

Reaction	Third body M	$A_r$ ( $\text{cm}^3 \text{mol}^{-1} \text{s}^{-1}$ )	$\beta_r$	$T_d$ (K)
$\text{CO}_2 + \text{M} \rightarrow \text{CO} + \text{O} + \text{M}$	$\text{CO}_2, \text{CO}, \text{N}_2, \text{O}_2, \text{NO}$	$6.9 \times 10^{21}$	-1.5	63275
	Ar	$6.9 \times 10^{20}$		
	C, N, O	$1.4 \times 10^{22}$		
$\text{CO} + \text{M} \rightarrow \text{C} + \text{O} + \text{M}$	$\text{CO}_2, \text{CO}, \text{N}_2, \text{O}_2, \text{NO}$	$2.3 \times 10^{20}$	-1.0	129000
	Ar	$2.3 \times 10^{19}$		
	C, N, O	$3.4 \times 10^{20}$		
$\text{N}_2 + \text{M} \rightarrow \text{N} + \text{N} + \text{M}$	$\text{CO}_2, \text{CO}, \text{N}_2, \text{O}_2, \text{NO}$	$7.0 \times 10^{21}$	-1.6	113200
	Ar	$7.0 \times 10^{21}$		
	C, N, O	$3.0 \times 10^{22}$		
$\text{O}_2 + \text{M} \rightarrow \text{O} + \text{O} + \text{M}$	$\text{CO}_2, \text{CO}, \text{N}_2, \text{O}_2, \text{NO}$	$2.0 \times 10^{21}$	-1.5	59750
	Ar	$3.0 \times 10^{21}$		
	C, N, O	$3.0 \times 10^{22}$		
$\text{NO} + \text{M} \rightarrow \text{N} + \text{O} + \text{M}$	$\text{CO}_2, \text{C}, \text{N}, \text{O}, \text{NO}$	$1.1 \times 10^{17}$	0.0	75500
	Ar	$5.0 \times 10^{15}$		
	$\text{CO}, \text{N}_2, \text{O}_2$	$5.0 \times 10^{15}$		
$\text{C}_2 + \text{M} \rightarrow \text{C} + \text{C} + \text{M}$	All	$2.0 \times 10^{21}$	-1.5	59750
$\text{NCO} + \text{M} \rightarrow \text{CO} + \text{N} + \text{M}$	All	$6.3 \times 10^{16}$	-0.5	24000
$\text{NO} + \text{O} \rightarrow \text{N} + \text{O}_2$		$8.4 \times 10^{12}$	0.0	19450
$\text{N}_2 + \text{O} \rightarrow \text{NO} + \text{N}$		$6.4 \times 10^{17}$	-1.0	38370
$\text{CO} + \text{O} \rightarrow \text{C} + \text{O}_2$		$3.9 \times 10^{13}$	-0.18	69200
$\text{CO}_2 + \text{O} \rightarrow \text{CO} + \text{O}_2$		$2.1 \times 10^{13}$	0.00	27800

latter contribution depends strongly on the surface catalytic properties of vehicle heat-shield [9].

Transport coefficient for pure species are derived from kinetic theory of gases; while the global transport properties of the gas mixture, semiempirical rules have been applied, such as the Wilke mixing rule for viscosity  $\mu$  and thermal conductivity  $\lambda$ . For the diffusion coefficient of the species  $i$ th in the reacting mixture, the multicomponent diffusion coefficient is applied [17].

The CFD analysis of the MBS has been preceded by a code validation phase performed considering the available numerical and experimental data for the Mars Pathfinder probe [7, 10]. To this end, the freestream conditions of Mars Pathfinder capsule at trajectory peak heating have been analysed.

As an example of the results provided by the validation phase, Figure 6 shows the Mach number contours comparison between the perfect gas and the equilibrium

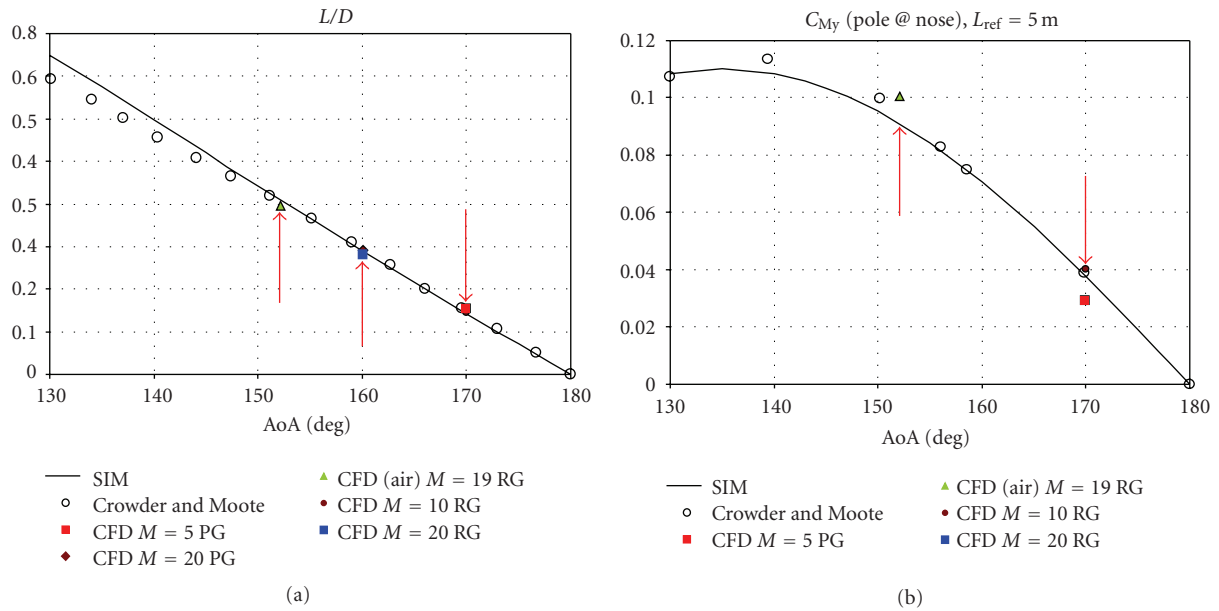


FIGURE 17:  $L/D$  ratio and pitching moment coefficients versus  $\alpha$ . Comparison among panel methods, CFD results, and experimental data [16].

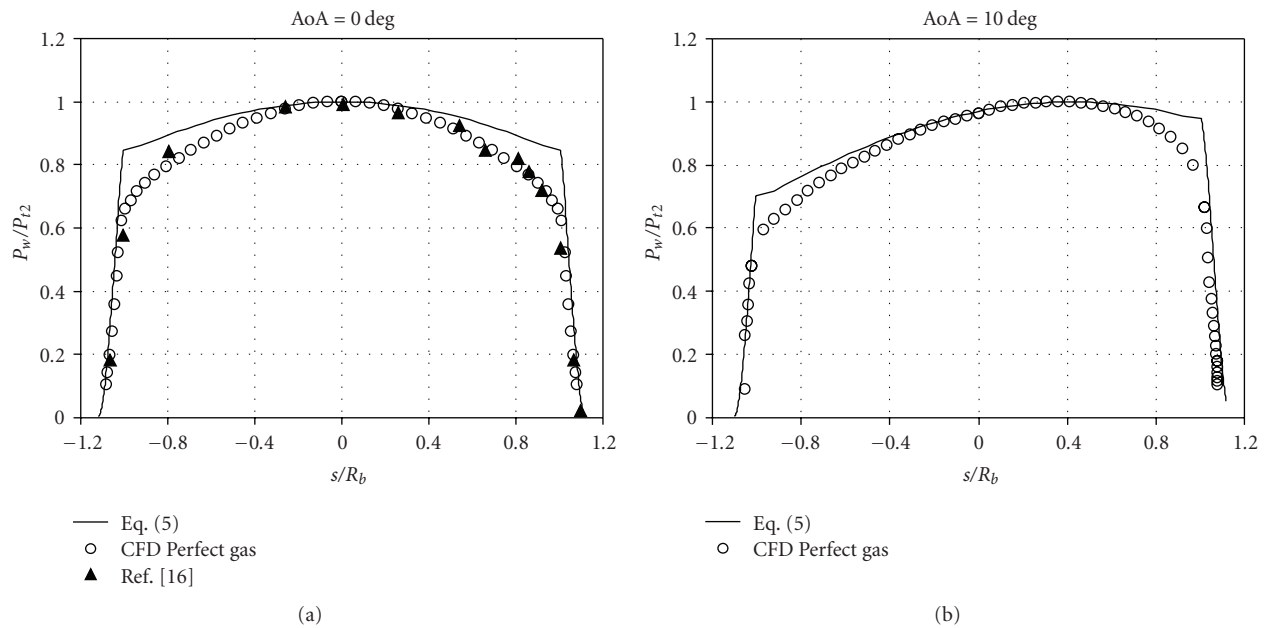


FIGURE 18: Pressure distribution in the capsule pitch plane for two AoAs (i.e., 0 and 10 deg). Comparison among MN, present CFD results, and WT data [16].

flow results. In order to appreciate the results difference, the flow field obtained in the case of perfect gas flow (upper side) and for equilibrium flow conditions (lower side) have been superimposed on the same figure. Figure 7 reports the same comparison but for the static temperature contours. Flow field streamlines are also shown in order to highlight the vortex structures which arise at the capsule lee side.

As one can see, both comparisons between perfect gas and equilibrium flow numerical computation underline that real gas effects markedly affect the flow field around the capsule and, hence, its aerodynamic performance. The effects of chemical dissociation can be recognized in Figure 8.

Finally, Figure 9 recognizes the comparison of surface pressure to stagnation pressure ratio between present computation and results of [7], as evaluated on the capsule center

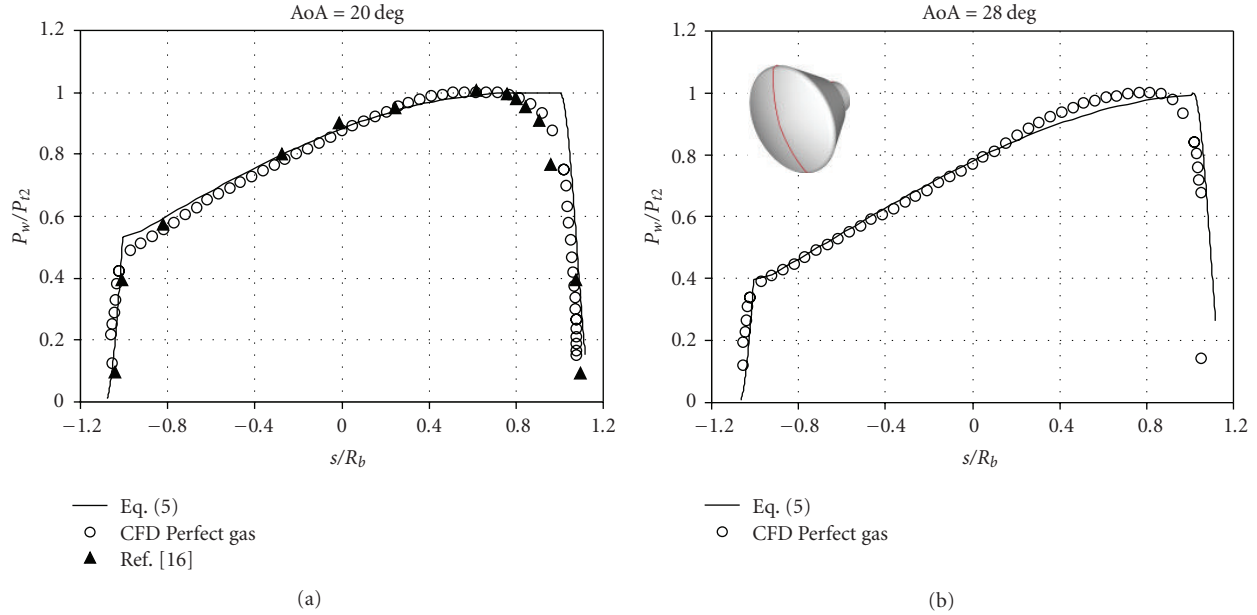


FIGURE 19: Pressure distribution in the capsule pitch plane for two AoAs (i.e., 20 and 28 deg). Comparison among MN, present CFD results, and WT data [16].

line. As shown, the comparison highlights a good agreement between numerical and experimental data.

Present CFD computations of MBS have been carried out on a multiblock structured grid (shown in Figure 10) generated by means of the commercial tool ICEM-CFD. The grid consists of 62 blocks for an overall number of 829,000 cells (half body) and is tailored for the freestream conditions summarized in Table 1.

The distribution of surface grid points has been dictated by the level of resolution desired in various areas of the vehicle, such as the stagnation region and the base fillet, according to the computational scopes. A close-up view of the 3D mesh on the vehicle surface can be seen on the right side of Figure 10. Grid refinement in strong gradient regions of flow field has been made through a solution-adaptive approach.

The results of CFD simulations are summarized hereinafter. For example, the flow field predicted around the MBS at  $M_\infty = 10$  and  $\alpha = 10 \text{ deg}$  can be appreciated in Figure 11, where the Mach number and static pressure fields are reported both on the capsule surface and pitch plane.

The same flow field features are reported in Figure 12 for  $M_\infty = 20$  and  $\alpha = 20 \text{ deg}$ . As shown, although the details of the flow vary with AoA and freestream conditions, the general features remain the same. For instance, when the MBS flies at high Mach number, a strong bow shock detaches in front of the entry vehicle and dominates the forebody flow field. In particular, the higher the Mach number, the narrower the shock layer and for  $M_\infty = 20$  and  $\alpha = 20 \text{ deg}$  the wake flow region is wider than that at  $M_\infty = 10$  and  $\alpha = 10 \text{ deg}$ , as expected.

In order to have an idea of the three-dimensional flow field that takes place past the entry capsule at  $M_\infty = 20$  and

$\alpha = 20 \text{ deg}$ , Figure 13 shows the static temperature contours on both capsule symmetry plane and two flow field cross-sections together with the static pressure contours on capsule surface, considering the Mars atmosphere as a perfect gas. As shown, the MBS bow shock structure around the descent vehicle can be well appreciated.

In Figure 13, one can realize as the separation shear layer coalesces, creating the “neck,” or narrowest point in the wake. Further, a shock forms at this point, called the neck or wake shock, which compresses the flow, leading to local maxima in temperature and pressure. Beyond the neck is the far wake, which extends for many body diameters downstream as the momentum deficit created by the passing capsule is slowly recovered. In a hypersonic flow, the wake is oriented parallel to the freestream velocity vector, as seen in Figure 13 [18]. Next results are reported in Figure 14, where the comparison between static temperature contours for perfect gas (a) and nonequilibrium gas computations (b) at  $M_\infty = 20$  and  $\alpha = 20 \text{ deg}$  is shown. Flow field streamlines are also reported in order to appreciate the complex flow pattern around the exploration vehicle.

For instance, as the flow turns around the capsule shoulder, it rapidly expands and can separate. The leeward side flow separates just after the shoulder whereas the windward side flow remains attached until the rear apex. The separated flow region is called the near wake. Further, a shear layer separates the outer flow from the recirculating inner core, which consists of multiple counter rotating vortices. The maximum flow field temperature in the case of perfect gas is close to about 40000 K. This means that thermochemical processes occur behind the bow shock as species vibrational excitation and dissociation. This is clearly shown by the maximum flow field temperature that, in the

case of nonequilibrium computation, reaches only about 8000 K. The contour fields of carbon dioxide and nitrogen which arises at  $M_\infty = 20$  and  $\alpha = 20$  deg are shown on the capsule pitch plane in Figure 15.

The curves of lift, drag, aerodynamic efficiency, and pitching moment coefficients are shown in Figures 16 and 17. Both those figures collect MBS aerodynamic coefficients compared with some experimental data, reported in order to highlight accuracy of engineering-based results [16]. As one can see, experimental and numerical data compare very well, thus confirming that engineering-based estimations represent a reliable preliminary aerodynamics of Mars entry capsule.

As shown, real gas effects increase both the aerodynamic drag and pitching moment coefficient, whereas the lift is only slightly influenced. Note that, Figures 16 and 17 report the Crowder-Moote and CFD results (CFD air  $M = 19$  RG) available for the Apollo capsule in air since, as said before, the static coefficients available for the air adequately represent the static coefficients for an aerodynamic braking vehicle in the Mars atmosphere [16].

The next set of comparisons, among CFD, experimental and numerical results, are reported in Figures 18 and 19. It displays the pressure ratio  $P_w/P_{t2}$  comparison, on the capsule pitch plane forward thermal shield, among present CFD results and wind tunnel (WT) experimental data provided in [16], for four AoA (i.e., 0, 10, 20 and 28 deg). Note that, CFD results refer only to perfect gas simulations considering that the stagnation-point pressure is essentially the same whether or not equilibrium is achieved. Furthermore, the real gas value is only slightly greater than the perfect gas value for a given freestream condition. Indeed, the stagnation-point pressure for hypersonic flow is (to first order) independent of the flow chemistry [17]. Experimental data, available only for  $\alpha = 0$  and 20 deg, refer to a test performed in the Tunnel C at Arnold Engineering and Development Centre (AEDC) at freestream Mach number of 10.18 and a Reynolds number  $R_{\infty D} = 1.1 \times 10^6$  [16]. As further comparisons note that the pressure distribution ( $P_w$ ) on the capsule center line can be evaluated considering that modified Newtonian (MN) theory states that

$$\frac{P_w}{P_{t2}} = \sin^2\theta + \frac{P_\infty}{P_{t2}} \cos^2\theta. \quad (5)$$

As one can see, numerical, experimental, and theoretical data compare well for all the AoAs, thus confirming reliability of the CFD simulations. Finally, it is worth noting that the differences existing between numerical and MN pressures, at the capsule corner (i.e.,  $s/R_b = 0.965$ ), are due to the vehicle forebody which is a truncated spherical cap. This means that the streamwise velocity gradients must be relatively large (i.e., above the value needed for a full hemisphere) in order to produce sonic flow at capsule corner [16].

## 5. Conclusion

The paper deals with the aerodynamic analysis of a manned braking system for Mars exploration mission. A number of

fully three-dimensional Navier-Stokes and Euler computational fluid dynamics simulations of the hypersonic flow field past an Apollo-shaped MBS have been performed in the framework of an entry loading environment compliant with the spacecraft released from a Mars circular parking orbit.

The range between Mach 2 and Mach 20 has been analyzed, with the goal to provide aerodynamic database at a Phase-A design level, for flight mechanics analyses. The aerodynamic coefficients have been provided as a function of Mach number and angle of attack (zero sideslip angle) according to the “space-based” design approach.

In the present analysis, only continuum regime (hypersonic speed ranges) with the flow modeled, both as perfect gas and reacting gas mixture, has been studied. Engineering-based analysis based on hypersonic panel methods has been extensively used in order to rapidly develop a very preliminary capsule aerodynamic database.

Finally, numerical results show that real gas effects increase both the aerodynamic drag and pitching moment coefficient whereas the lift is only slightly influenced. Moreover, several results comparisons highlight that experimental and CFD aerodynamic findings available for the Apollo capsule in air adequately represent the static coefficients of the MBS in the Mars atmosphere.

## Nomenclature

$C_D$ :	Drag coefficient
$C_L$ :	Lift coefficient
$C_{My}$ :	Pitching moment coefficient
$C_p$ :	Pressure coefficient
$D$ :	Aerodynamic drag, N
$F$ :	Aerodynamic force, N
$L$ :	Aerodynamic lift, N
$M$ :	Mach number/aerodynamic moment, Nm
$P$ :	Pressure, Pa
$q$ :	Dynamic pressure, Pa
$R$ :	Radius of curvature, m
Re:	Reynolds number
$S$ :	Reference area, m <sup>2</sup> .

## Greek Symbols

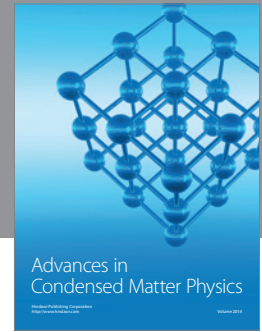
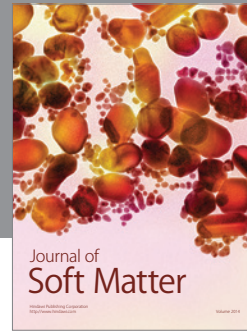
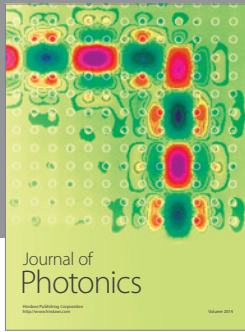
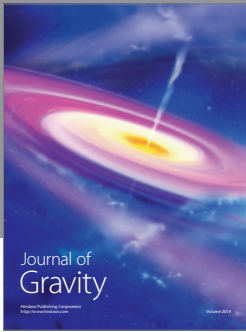
$\alpha$ :	Angle of attack, deg
$\rho$ :	Density, kg/m <sup>3</sup>
$\gamma$ :	Specific heats ratio.

## Subscripts

$b$ :	Base
ref:	Reference
$t2$ :	Stagnation point downstream a normal shock
$w$ :	Wall
$Y$ :	Pitching moment
$\infty$ :	Freestream conditions.

## References

- [1] B. Drake, "Mars Human Exploration Reference Mission," LPI Contribution no. 955.
- [2] G. Polishchuk, K. Pichkhadze, V. Vorontsov, and K. Pavel, "Proposal on application of Russian technical facilities for International Mars Research Program for 2009–2015," *Acta Astronautica*, vol. 59, no. 1–5, pp. 113–118, 2006.
- [3] D. Wilde and S. Walther, "Inflatable reentry and descent technology (IRDT)—further developments," in *Proceedings of the 2nd International Symposium of Atmospheric Reentry Vehicles and Systems*, Arcachon, France, March 2001.
- [4] O. M. Alifanov, V. I. Outchvatov, and K. M. Pichkhadze, "Thermal protection of re-entry vehicles with the usage of inflatable systems," *Acta Astronautica*, vol. 53, no. 4–10, pp. 541–546, 2003.
- [5] A. Mack, "CFD validation for CO<sub>2</sub> reentry applications," in *Proceedings of the 2nd International ARA Days*, Arcachon, France, 2008.
- [6] A. Viviani, G. Pezzella, and C. Golia, "Aerothermodynamic analysis of a capsule vehicle for manned exploration missions to Mars," in *Proceedings of the 27th Congress of the International Council of the Aeronautical Sciences (ICAS '10)*, Nice, France, 2010.
- [7] R. A. Mitcheltree and P. A. Gnoffo, "Wake flow about the Mars Pathfinder entry vehicle," *Journal of Spacecraft and Rockets*, vol. 32, no. 5, pp. 771–776, 1995.
- [8] D. K. Prabhu, "System design constraints-trajectory aerothermal environments," in *Critical Technologies for Hypersonic Vehicle Development*, RTO AVT/VKI Lecture Series, Von Karman Institute for Fluid Dynamics, Rhode Saint Genèse, Belgium, 2004.
- [9] J. D. Anderson, *Hypersonic and High Temperature Gas Dynamics*, McGraw-Hill, New York, NY, USA, 1989.
- [10] P. Gnoffo, R. Braun, K. Weilmuenster, R. Mitcheltree, W. Engelung, and R. Powell, "Prediction and validation of Mars Pathfinder hypersonic aerodynamic data base," in *Proceedings of the 7th AIAA/ASME Joint Thermophysics and Heat Transfer Conference*, Albuquerque, NM, USA, 1998.
- [11] P. A. Gnoffo, K. J. Weilmuenster, R. D. Braun, and C. I. Cruz, "Influence of sonic-line location on Mars Pathfinder Probe aerothermodynamics," *Journal of Spacecraft and Rockets*, vol. 33, no. 2, pp. 169–177, 1996.
- [12] R. N. Gupta, K. P. Lee, and C. D. Scott, "Aerothermal study of Mars Pathfinder aeroshell," *Journal of Spacecraft and Rockets*, vol. 33, no. 1, pp. 61–69, 1996.
- [13] C. Park, J. T. Howe, R. L. Jaffe, and G. V. Candler, "Review of chemical-kinetic problems of future NASA missions—II: Mars entries," *Journal of Thermophysics and Heat Transfer*, vol. 8, no. 1, pp. 9–22, 1994.
- [14] V. Hannemann and A. Mack, "Chemical non equilibrium model of the Martian atmosphere," in *Proceedings of the 6th European Symposium on Aerothermodynamics for Space Vehicles*, ESA, Versailles, France, 2008, ESA SP-659.
- [15] E. V. Kustova, E. A. Nagnibeda, Y. D. Shevelev, and N. G. Syzranova, "Comparison of non-equilibrium supersonic CO<sub>2</sub> flows with real gas effects near a blunt body," in *Proceedings of the 6th European Symposium on Aerothermodynamics for Space Vehicles*, ESA, Versailles, France, 2008, ESA SP-659.
- [16] R. S. Crowder and J. D. Moote, "Apollo entry aerodynamics," *Journal of Spacecraft and Rockets*, vol. 6, no. 3, pp. 302–307, 1969.
- [17] J. J. Bertin, *Hypersonic Aerothermodynamics*, AIAA Education Series, AIAA, Washington, DC, USA, 1994.
- [18] M. J. Wright, F. S. Milos, and P. Tran, "Afterbody aeroheating flight data for planetary probe thermal protection system design," *Journal of Spacecraft and Rockets*, vol. 43, no. 5, pp. 929–943, 2006.



**Hindawi**

Submit your manuscripts at  
<http://www.hindawi.com>

